Petroleum Science 23 (2026) 262–277

Contents lists available at ScienceDirect

Petroleum Science

journal homepage: www.keaipublishing.com/en/journals/petroleum-science

Original Paper

In-situ pressure-preserved coring for deep resources exploration: A novel pressure sealing subsystem and its service performance

Da Guo [a,b,c], Ling Chen [a,b], Jia-Nan Li [a], Le Zhao [c], Yi-Wei Zhang [a,c], Ding-Ming Wang [a,c], Xin Fang [a,c], Zhi-Qiang He [c], Lin Dai [d], He-Ping Xie [a,c,*]

[a] State Key Laboratory of Intelligent Construction and Healthy Operation and Maintenance of Deep Underground Engineering, Sichuan University, Chengdu, 610065, Sichuan, China
[b] School of Mechanical Engineering, Sichuan University, Chengdu, 610065, Sichuan, China
[c] State Key Laboratory of Intelligent Construction and Healthy Operation and Maintenance of Deep Underground Engineering, Sichuan University, Shenzhen, 518060, Guandong, China
[d] Petroleum Engineering Technology Research Institute of Sinopec Jianghan Oilfield Company, Wuhan, 430035, Hubei, China

ARTICLE INFO

Article history:
Received 28 March 2025
Received in revised form
30 October 2025
Accepted 30 October 2025
Available online 4 November 2025

Edited by Jia-Jia Fei

Keywords:
Deep mining
In-situ rock mechanics
Pressure coring
Deep resources exploration
Onshore drilling

ABSTRACT

In-situ pressure coring technology is a responsible exploration technique for enhancing the efficiency and capacity of deep resources development. However, reliability issues in pressure sealing introduce significant uncertainty in field applications of this technology. This work presents a novel pressure sealing subsystem within the in-situ pressure-preserved coring system to overcome the inherent problem. The design concept and structure composition of the pressure sealing subsystem are described. To enhance pressure sealing reliability in real downhole conditions, the subsystem incorporates a dynamic sealing structure between the inner tube and the pressure bearing tube, and a close-fitting sealing face between the pressure controller and the bottom of the inner tube. Theoretical calculations and computational fluid dynamics (CFD) simulations were conducted to evaluate the mechanical behavior and fluid flow characteristics within the pressure sealing subsystem, determining the structural effects on performance. A smaller pump displacement during inner tube lifting and a moderate overflow hole diameter of 7 mm enhance the success rate of a sequence of mechanical actions required for the in-situ pressure sealing. Numerical, laboratory, and field tests were conducted to verify the service performance. Numerical analysis indicates that the particle settlement ratio in the novel structure is only 32% of that in the original design. In laboratory downhole circulation and drilling tests, the pressure sealing subsystem successfully maintained an in-situ pressure of 0.2 MPa at a depth of approximately 9–10 m. In field applications, a 1.95 m in-situ core sample was retrieved at 22 MPa from a depth of approximately 1970 m.

1. Introduction

Implementing a more efficient and environmentally sustainable approach to the exploration and extraction of energy and mineral resources can effectively mitigate the tension between the escalating demand for energy and the increasingly pressing environmental issues (Xie et al., 2020). Due to the depletion of shallow resources, the focus of the development of energy and mineral resources is progressively shifting towards the deep well (Li et al., 2025; Xie et al., 2023). The development of deep resources relies on a full understanding of the laws governing resource generation and rock mechanics in the target layer (Xie et al., 2021a). To gain insights into these laws, it is essential to extract deep core samples from the target layer and conduct tests on the core (Guo et al., 2023a). Conventional coring obtains the deep core by non-pressurized core barrels, as shown in Fig. 1(a), due to significant mechanical disturbances and pressure reduction during core recovery, the mechanical, physical, and chemical properties of the core undergo changes in their in-situ state. These changes include alterations in gas-solid-liquid equilibrium, fluid solubility, and the

* Corresponding author.
E-mail address: xiehp@szu.edu.cn (H.-P. Xie).
Peer review under the responsibility of China University of Petroleum (Beijing).

https://doi.org/10.1016/j.petsci.2025.10.031

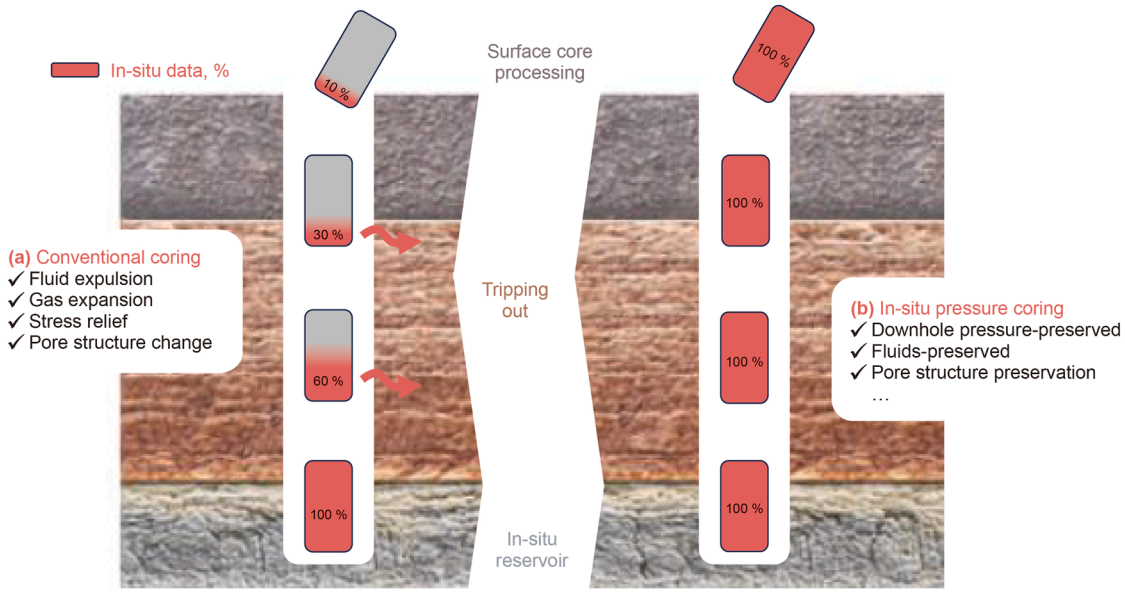

Fig. 1. Comparison of the conventional coring with the in-situ pressure coring technology. % means the condition of the obtained core sample compared with that in the in-situ reservoir.

structural integrity of the core (Ashena and Thonhauser, 2018). Consequently, it is compelled to consider these changes when analyzing and testing cores obtained by conventional methods. This means that the subsurface data obtained from conventional coring techniques must be corrected by theoretical formulas. Unfortunately, this correction is not accurate enough due to the change in the in-situ characteristics of the core (Xie et al., 2021b).

As shown in Fig. 1(b), in-situ pressure coring technology can overcome the above limitations and provide in-situ subsurface data that is not obtainable by other means (Mukherjee et al., 2019), by obtaining the core samples with in-situ pressure. These pressure-preserved cores, in their in-situ reservoir state, offer a unique view to elucidate the real in-situ formation characteristics by direct measurement rather than estimation, including the in-situ rock mechanics characteristics, core saturation, fluid proportion, porosity, permeability, and the physical and chemical characteristics of the reservoir. By using the in-situ pressure coring technology, an accurate assessment of reservoir geological conditions and reserves scale can be achieved, leading to improved exploration and development efficiency (Hu et al., 2022).

Currently, extensive studies have been conducted in the last few decades on pressure coring technology, leading to the development of various pressure coring tools. The pressure core barrel (PCB) utilized in the deep sea drilling project (DSDP) is derived from the wireline coring technique, with a pressure-preserved capacity of about 35 MPa (Kvenvolden et al., 1983). The pressure core sampler (PCS) developed by the ocean drilling program (ODP) has a maximum design sealing pressure of 70 MPa, but its practical field application does not exceed 30 MPa (Dickens et al., 1997, 2003). The hydrate coring equipment system (HYACE), designed by the European Union, consists of the impact sampler Fugro pressure corer (FPC) and the bottom-of-hole power rotary sampler, HYACE rotary corer (HRC), with a maximum pressure-preserved capacity of 25 MPa (Schultheiss et al., 2009). The National Oil and Gas Corporation (NOG) of Japan developed a pressure temperature core sampler (PTCS), with a pressure-preserved capacity of 25 MPa (Kawasaki et al., 2006). In Germany, multiple autoclave corer (MAC) and dynamic autoclave piston corer (DAPC) were developed in 2002 and 2003, but their maximum pressure-preserved capacity was less than 20 and 14 MPa, respectively (Abegg et al., 2008; Jackson et al., 2017). Geotek company developed a pressure coring tool with ball valve (PCTB) and high pressure temperature corer (HPTC) for natural gas hydrate exploration, which has a pressure-preserved capacity of 35 MPa (Schultheiss et al., 2017; Thomas et al., 2020). In China, Zhejiang University developed the pressure tight piston corer (PTTC), with a maximum pressure-preserved capacity of 25 MPa (Qin et al., 2005). China University of Petroleum (Beijing) developed a pressure and temperature preservation system (PTPS), with a pressure-preserved capacity of less than 30 MPa (Zhu et al., 2013). Additionally, CNPC Greatwall Drilling Company developed the GWY194-70BB and GW-CP194-80A coring tools, with the latter having a higher pressure-preserved capacity of 60 MPa (Yang et al., 2014, 2020). Jilin University proposed an innovative approach using liquid-solid phase transitions to achieve sealing and pressure preservation to overcome the sealing failure problem caused by the solid-phase particles in the drilling fluid (Luo et al., 2015). However, this method is only suitable for the low-temperature environment of deep-sea hydrate coring, and the pressure resistance of the freeze-core valve formed by it does not exceed 43 MPa. Similarly, to improve the reliability of pressure coring, Jilin University and the Chinese Academy of Geological Sciences developed a pressure core sampler for marine gas hydrate exploration. This tool achieves the initial pressure-preserved sealing by utilizing the self-weight of the core barrel. In eight pressure coring operations conducted at three different offshore wells, a success rate of 87.5% was achieved (Li et al., 2021a, 2024). However, the pressure resistance of this tool is only 32.1 MPa. In addition, for the requirements of subsea sediment sampling, Hunan University of Science and Technology developed the “Hainiu” seabed drilling rig. This system adopts a two-step sealing mechanism to maintain in-situ pressure: first, the corer is retrieved to the seabed surface, and then a robotic arm secures a threaded sealing cap, thereby enhancing operational reliability (Wang et al., 2022a, 2022b, 2023). Furthermore, a full-ocean-depth pressure core sampling device has also been developed, which has demonstrated promising application performance (Liu et al., 2023a, 2023b, 2025).

Although the existing pressure coring technologies have been robust in the past few decades, the pressure-preserving limit of current pressure coring technologies is usually less than 70 MPa, which makes it difficult to adapt to the needs of deeper exploration. The main limitation is the sealing performance of the pressure sealing subsystem at the bottom of the coring tool. This subsystem is tasked not only with facilitating core passage during coring but also with achieving pressure sealing at the bottom through a series of mechanical actions after coring. Consequently, the structure of the pressure sealing subsystem is exceedingly complex, and it is challenging to enhance its pressure retention capacity due to the confined space in the wellbore. To address this issue, our team has designed an innovative valve based on the Steinmetz solid structure in the pressure sealing subsystem and named the pressure controller (Xie et al., 2023). And, a lot of research has been carried out to explore the principle and method of pressure coring in the laboratory based on the pressure controller (Li et al., 2021b, 2022). To improve the pressure-preserved capacity of the pressure controller, the pressure bearing ability and the failure form of the pressure controller were studied by numerical simulation (Li et al., 2021b). Further, the optimized structure of the pressure controller was determined and the ultimate pressure sealing capacity can reach 140 MPa in the laboratory pressure tests (Xie et al., 2024). Despite the pressure controller in the pressure sealing subsystem being designed to withstand extremely high pressure, practical implementation, particularly in deep oil and gas drilling sites, has presented several challenges: (1) The complex hole structure and confined wellbore space make it challenging for the pressure controller integration. (2) During downhole pressure coring operations, a sequence of mechanical actions must be conducted to close the pressure controller and achieve sealing. However, conducting these actions in the real drilling fluid, which has higher density and viscosity, requires overcoming greater liquid resistance compared to an ideal air or water environment. (3) During coring, drilling fluid carrying solid phases circulates within the pressure coring tool. Solid particles may settle to the sealing interface of the pressure controller or the assembly space of the components, resulting in mechanical action failure and consequent sealing leakage issues.

However, as shown in Fig. 2, previous research primarily has concentrated on the pressure bearing and sealing capacities of the pressure controller (Li et al., 2021b, 2022). The primary limitation is the neglect of the actual service status of the pressure controller in downhole drilling fluid environments. This work innovated a pressure sealing subsystem aimed at achieving the on-site integrated application of a pressure controller and increasing the success rate of pressure sealing. Theoretical calculations and computational fluid dynamics (CFD) simulations were utilized to assess the mechanical behavior and fluid flow characterization within the pressure sealing subsystem, enabling the determination of the effects of the subsystem structure on the service performance. The structure parameters and technique process of the pressure sealing subsystem were determined and verified by laboratory tests and field application.

2. Design of the pressure sealing subsystem

2.1. General design concept of the pressure sealing subsystem

Pressure coring technology offers a promising solution for accurately determining storage resources in deep exploration. To meet this demand, we have designed an in-situ pressure-preserved coring system (IPP-coring system), whose structure and the schematic diagrams in the drilling and recovering process are detailed in Fig. 3(a) and (b), respectively. The specific design and detailed working principle of the IPP-coring system is not in the scope of this paper and can be referred to (Guo et al., 2023b, 2024). From Fig. 3(b), the IPP-coring system with the pressure sealing subsystem as its core component maintains the in-situ pressure by forming a sealed pressure vessel downhole. The working process of the pressure sealing subsystem is shown in Fig. 3(c). The subsystem not only facilitates core passage during coring but also ensures pressure sealing at the bottom through a series of mechanical actions. It mainly consists of a spring, an inner tube, pressure bearing tubes, and a pressure controller. The pressure

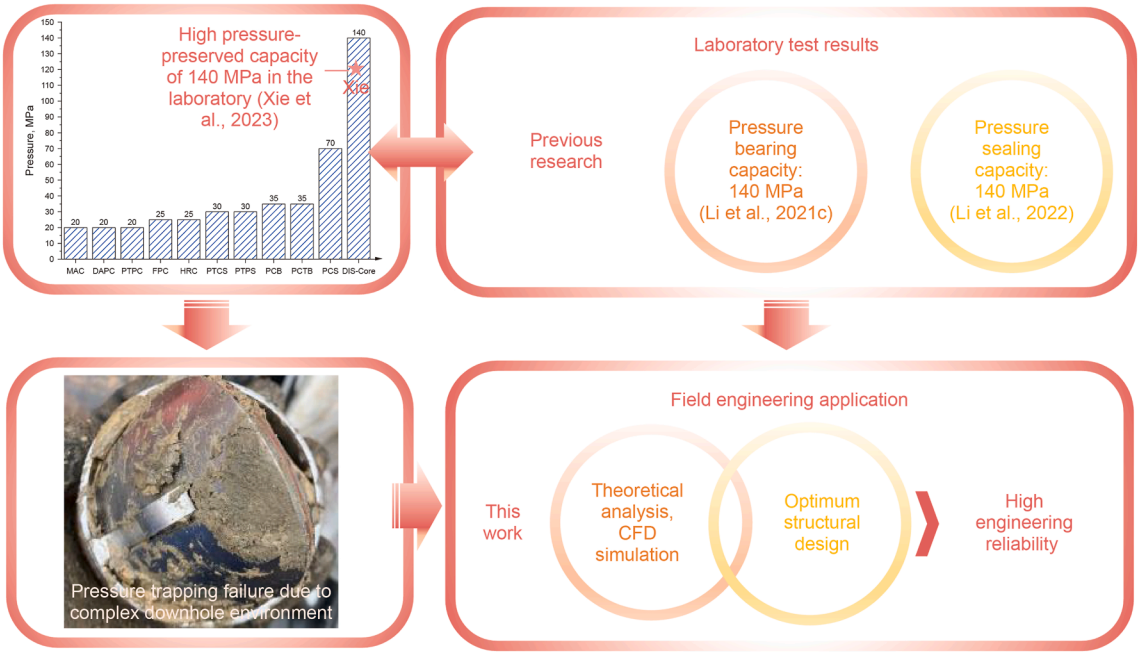

Fig. 2. Highlights of this work compared with the previous research.

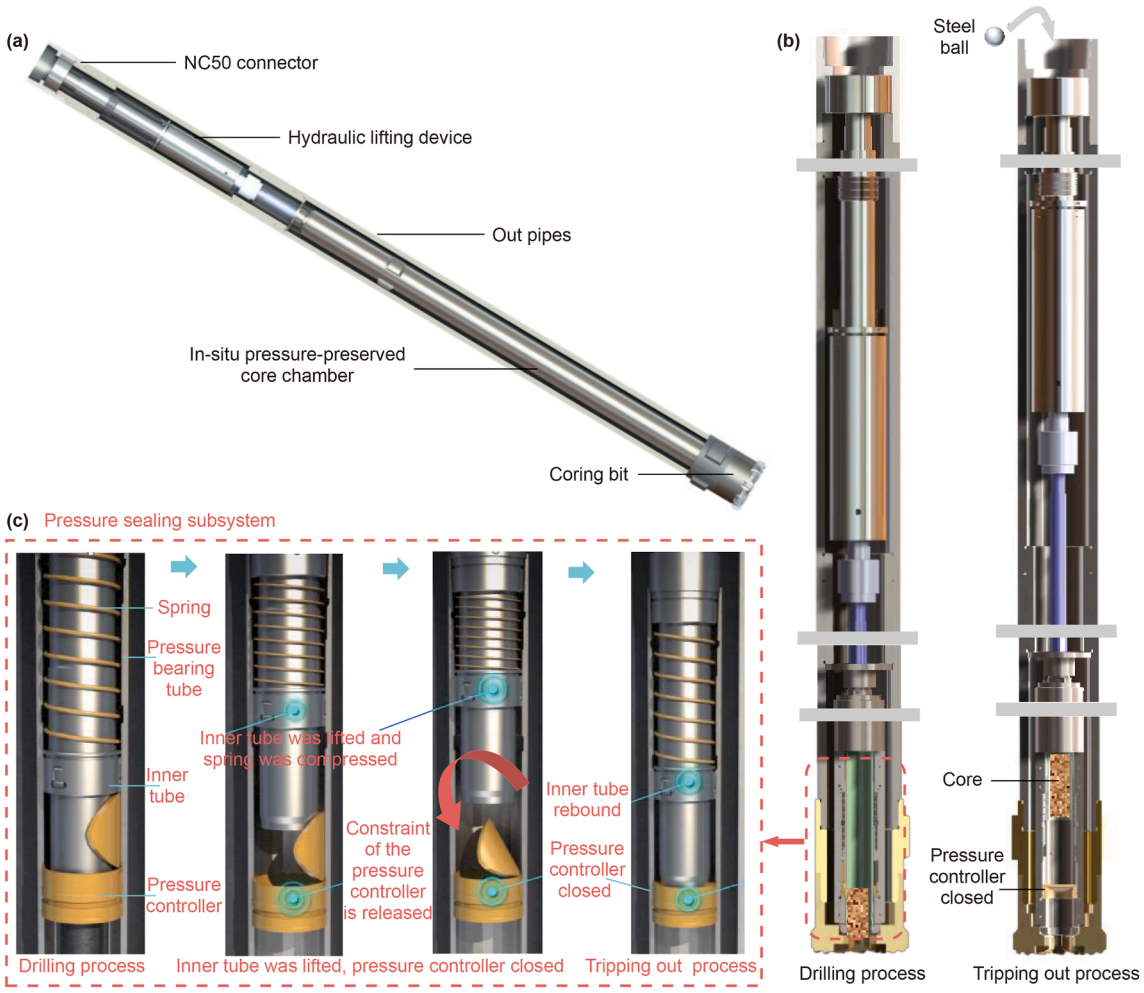

Fig. 3. (**a**) The basic structure of the IPP-coring system; (**b**) the schematic diagrams of the IPP-coring system in the drilling and recovering process; (**c**) the general design concept diagram and the pressure sealing principle of the pressure sealing subsystem.

sealing process consists of four steps: (1) Core enters the IPP-coring system, and it is cut by lifting the drill strings. (2) The inner tube is lifted under liquid pressure following a command from a steel ball, simultaneously compressing the spring. (3) Once the inner tube is lifted over the pressure controller, the constraint is released, allowing the pressure controller to close under gravity. (4) After the inner tube is lifted to the unlocked position, it no longer continues to move upward and rebounds downward under the force of the compressed spring. Subsequently, the inner tube is pressed against the closed pressure controller to apply an initial sealing load. After the above sequence of mechanical action, the in-situ pressure sealing is realized downhole. Due to the complex downhole environment, the pressure sealing subsystem faces two inherent problems. Firstly, due to the compact internal structure of the IPP-coring system, the inner tube will be subjected to great liquid resistance when it is lifted. Excessive resistance may prevent the inner tube from reaching the unlocking position, leading to pressure sealing failure. Secondly, drilling fluid will likely carry particles into the subsystem, causing leakage or mechanical failure by adhering to the sealing surface or accumulating in the annulus within the inner tube and the pressure bearing tube.

To overcome the above inherent problems, a novel pressure sealing subsystem is further designed for the demanding downhole environment. As shown in Fig. 4(a)–(c), to minimize particle intrusion into key parts of the pressure sealing subsystem, the mechanical fit relationship and structural features of the inner tube, the core tube, and the pressure controller are carefully designed: (1) A dynamic sealing structure with two sealing rings was implemented within the inner tube and the pressure bearing tube to prevent direct particle intrusion into the annular space of the inner tube. The two sealing rings are made of fluorine rubber, which exhibits high temperature and corrosion resistance. (2) The bottom of the inner tube is designed to fit closely with the sealing face of the pressure controller, minimizing the adherence of the particles to the sealing surface. (3) To reduce the resistance of the inner tube lifting process, two flow holes are incorporated into its sidewall to maintain pressure balance.

2.2. Kinematic resistance analysis in the pressure sealing subsystem

The success of the in-situ pressure sealing depends on the performance of the pressure sealing subsystem. However, the working process of this subsystem in the complex downhole environment cannot be directly observed, which is different from the ideal air or clean water environment in the laboratory, making it challenging for the targeted design of this subsystem. Therefore, a deep analysis of the working process and the kinematic resistance of the pressure sealing subsystem in the drilling fluid environment is essential.

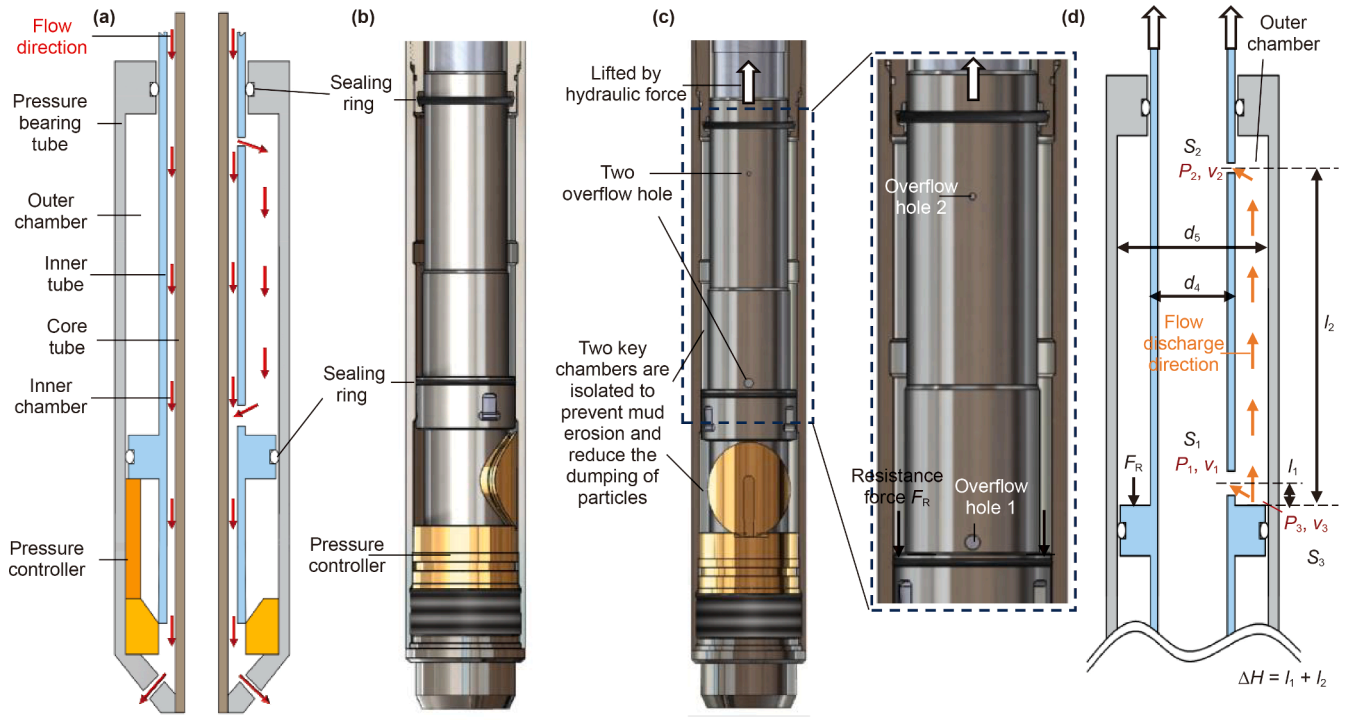

Fig. 4. Schematical diagram of the pressure sealing subsystem: (**a**) the flow path of the drilling fluid during core drilling process, (**b**) the front view and (**c**) side view of the pressure sealing subsystem, (**d**) the discharge of the fluid in the pressure sealing subsystem.

As shown in Fig. 4(c) and (d), when lifting the inner tube to conduct the sequence of mechanical action for realizing the pressure sealing, the lifting force F_{lif} should meet the following requirements:

$$F_{lif} \geq F_R = F_g + F_{fR} + F_{hR} + F_{sR} \tag{1}$$

where F_R is the total resistance, F_g is gravity, F_{fR} is the friction resistance of the two sealing rings, F_{hR} is the hydraulic resistance, F_{sR} is the resistance of the spring. Among them, the gravity of the inner tube is about 17.15 N. The friction resistance of the sealing ring can be calculated using the following formula (Al-Ghathian et al., 2005):

$$F_{fR} = \mu\pi d_{ss} d_{so} E\left(1 - \frac{|d_{ss} - d_{io}|}{2d_{so}}\right)\sqrt{1 - \frac{(d_{ss} - d_{io})^2}{4{d_{so}}^2}} \tag{2}$$

where μ represent the coefficient of friction between the O-ring and sealed surface, d_{ss} is the diameter of the sealed surface, E is the elastic modulus of the O-ring, d_{io} is the inside diameter of the O-ring groove, and d_{so} is the section diameter of the O-ring. The total friction of the sealing ring is calculated as 131 N, based on the specific structural parameters of the sealing surface.

In addition, the resistance of the spring can be calculated (Xu et al., 2022):

$$F_{sR} = k\Delta x \tag{3}$$

where k is the stiffness of the spring, Δx is the displacement of the spring, and the stiffness of the spring can be calculated (Huang et al., 2023):

$$k = \frac{G \cdot d_{sw}^4}{8 \cdot e \cdot d_{sm}^3} \tag{4}$$

where G is the shear modulus of the spring material at room temperature, d_{sw} is the spring wire diameter, e is the effective number of the spring, d_{sm} is the spring middle diameter.

To provide sufficient initial sealing force for the pressure controller, the spring is elaborately selected. The material of the selected spring is carbon steel with a shear modulus G of 79,000 MPa. It has an effective number n of 18, and the spring wire diameter d_{sw} and the spring middle diameter d_{sm} are 4 and 65 mm, respectively. And the initial resistance of the spring is 113.4 N.

Compared with the friction resistance of the seal ring and the resistance of the spring, the resistance generated by the drilling fluid is dominant in the limited space of the pressure sealing subsystem. As shown in Fig. 4(c) and (d), a dynamic sealing structure is formed by the inner tube, the pressure bearing tube, and two sealing rings. When the inner tube was lifted by the liquid pressure to conduct a sequence of mechanical actions to realize the in-situ pressure sealing, as shown in Fig. 4(d), the volume of the outer chamber would be compressed. At this time, the fluid inside the cavity is expelled through two overflow holes, namely, overflow holes 1 and 2 shown in Fig. 4(c) and (d). According to the continuity equation, the fluid inside the outer chamber satisfies (Yang, 2008):

$$v_a s_a = v_b s_b \tag{5}$$

where v_a and v_b represent the average flow velocities at cross-sections a and b, respectively; and s_a and s_b denote the corresponding cross-sectional areas.

Assuming that the fluid inside the chamber is incompressible, when the inner tube is lifted, the internal fluid also satisfies the Bernoulli equation (Kundu et al., 2015):

$$Z_a + \frac{P_a}{\rho g} + \frac{\alpha_a v_a^2}{2g} = Z_b + \frac{P_b}{\rho g} + \frac{\alpha_b v_b^2}{2g} + \sum h_f + \sum h_l \tag{6}$$

where Z_a and Z_b represent the surface potential energies at cross-sections a and b, P_a and P_b represent the corresponding local pressures. The fluid density is given by ρ. α_a and α_b are the kinetic energy correction factors, they are 1 and 2 in the turbulent and laminar flow systems, respectively (Li, 2012). h_f and h_l are the frictional head loss and the local head loss, respectively (Wang et al., 2023), g is gravitational acceleration. Due to the high lifting velocity and the corresponding high Reynolds number of the fluid in the outer chamber, the flow is usually turbulent; therefore, α_a and α_b are both 1.

In this study, to simplify the calculation, the pressure and velocity at the outlet of the cavity (P_1 and v_1 in overflow hole 1 and P_2 and v_2 in overflow hole 2, shown in Fig. 4) are set to be equal. Assuming that the fluid inside the chamber is incompressible, the fluid velocity v_3 at section s_3, shown in Fig. 4, is approximately equal to the hydraulic lifting velocity. According to (Guo et al., 2024), v_3 and pump displacement Q satisfy the following relation:

$$v_3 = \frac{Q}{4.4} \tag{7}$$

Therefore, according to Eqs. (5)–(7), the fluid pressure difference ΔP caused by the lifting of the inner tube satisfies:

$$\Delta P = \frac{\rho Q^2}{38.72}\left[\left(\frac{s_3}{s_1 + s_2}\right)^2 - 1\right] + \rho g\left(\sum h_f + \sum h_l + \Delta H\right) \tag{8}$$

where s_1 and s_2 are the areas of overflow hole 1 and 2, respectively; s_3 represents the area of the drainage annulus shown in Fig. 4; ΔH is the sum of the distances from section s_1 to sections s_2 and s_3. The frictional head loss and the local head loss are satisfied by the following equations (Wang et al., 2023):

$$h_f = \lambda \frac{L}{d_{ae}} \cdot \frac{v_{flu}^2}{2g} \tag{9}$$

$$h_l = \xi \cdot \frac{v_{flu}^2}{2g} \tag{10}$$

where λ represents the frictional loss factor, L denotes the pipe length, d_{ae} represents the annulus equivalent diameter, v_{flu} is the fluid velocity, and ξ is the local loss coefficient. The frictional loss factor λ under turbulent flow conditions can be determined as follows (Vakkilainen, 2017):

$$\lambda = \frac{0.3164}{Re^{0.25}} \tag{11}$$

where Re is the Reynolds number. In this study, the drilling fluid was considered a Newtonian fluid, and it satisfies (Kundu et al., 2015):

$$Re = \frac{\rho v_{flu} d_{ae}}{\eta} \tag{12}$$

where η is the kinetic viscosity of the drilling fluid, and d_{ae} is the annulus equivalent diameter, it satisfies (Kundu et al., 2015):

$$d_{ae} = \frac{4S}{\chi} \tag{13}$$

where S is the annular section area and χ is the wetting perimeter, and it was calculated:

$$d_{ae} = d_5 - d_4 \tag{14}$$

where d_4, d_5 are the diameters shown in Fig. 4, from Eqs. (9)–(14), the total frictional head loss can be calculated:

$$\sum h_f = \frac{0.158 \Delta H v_3^{1.75} \eta^{0.25}}{\rho^{0.25}(d_5 - d_4)^{1.25} g} = \frac{0.0248 \Delta H Q^{1.75} \eta^{0.25}}{\rho^{0.25}(d_5 - d_4)^{1.25} g} \tag{15}$$

The local head loss coefficient at the sharp turn bay is 1.1 (Kleinstreuer, 2018), then the total local head loss at the outlet (overflow holes 1 and 2) satisfies:

$$\sum h_l = 1.1 \cdot \frac{v_1^2}{g} \tag{16}$$

According to Eqs. (5), (7) and (16), the total local head loss at the outlet (overflow holes 1 and 2) can be calculated according to pump displacement:

$$\sum h_l = \frac{0.057 Q^2 s_3^2}{g(s_1 + s_2)^2} \tag{17}$$

In addition, the hydraulic resistance satisfies:

$$F_{hR} = \Delta P \cdot s_3 \tag{18}$$

Thus, according to Eqs. (8), (15), (17) and (18), the hydraulic resistance can be calculated.

After coring, the core tube lifts the inner tube via three pins under the hydraulic force. Considering the strength of the pins (Kumar et al., 2015), the lifting resistance should not exceed the strength of the pins:

$$F_{lif} < F_{she} = \frac{\tau_{she} S_{she}}{n} \tag{19}$$

where n is the safety factor, F_{she} is the maximum total shear force, s_{she} is the shear sectional area, τ_{she} is the shear strength of the C63000 Nickel Aluminum Bronze of about 427–483 MPa (measured at room temperature, 20 °C).

The safety factor was set as 2, the maximum total shear force of the three pins can be calculated:

$$F_{she} = \frac{\tau_{she} S_{she}}{n} = 22.9 \text{ kN} \tag{20}$$

From the flow direction (red arrow) shown in Fig. 4(a), drilling fluid circulates from the overflow hole 2 to the overflow hole 1 during core drilling. Therefore, to avoid the direct injection of the solid phase in the drilling fluid to the outer chamber, the diameter of overflow hole 2 was maintained, while efforts were made to reduce total resistance F_R in the lifting process of the inner tube by adjusting the diameter of overflow hole 1. The variations of the total resistance force F_R with the pump displacement, which was calculated by Eq. (1), in different diameters of the overflow hole 1 and the drilling fluid density when the drilling fluid viscosity was 100 mPa·s are shown in Fig. 5(a–d). It can be found that: (1) An increase in drilling fluid density leads to a significant rise in resistance. For instance, with the drilling fluid density rising from 1300 to 1700 kg/m^3 when the diameter of the overflow hole 1 is 4 mm and the drilling displacement is 30 L/s, the total resistance increases 31% from 147 to 192 kN. (2) Increasing the diameter of

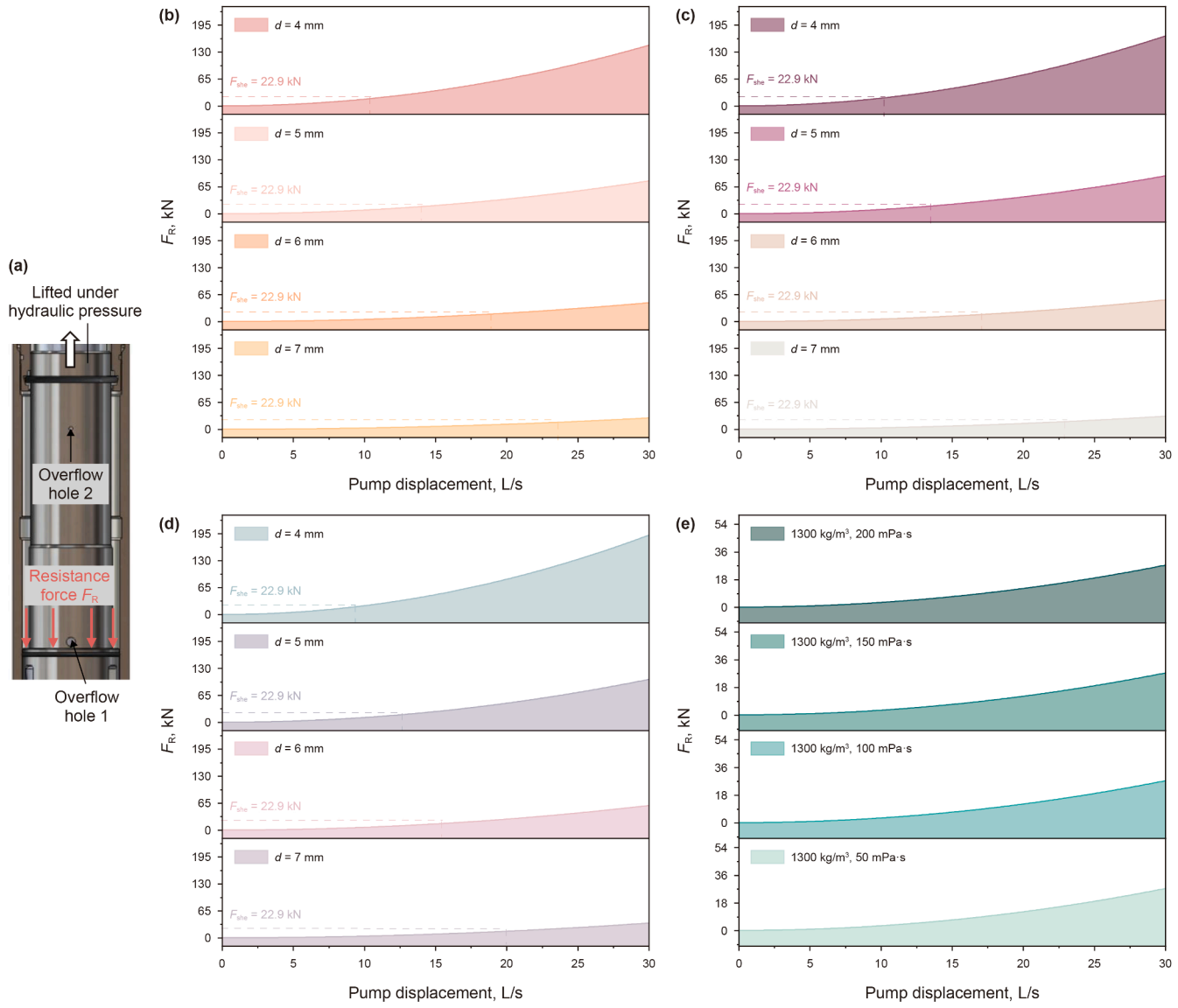

Fig. 5. (**a**) Schematic diagram shows the resistance force of the inner tube when the mechanical action for pressure sealing was conducted; (**b**–**d**) the variation of the total resistance force with the pump displacement in different diameters of the overflow hole 1 and the drilling fluid density, (**b**) 1300, (**c**) 1500 and (**d**) 1700 kg/m^3, when the drilling fluid viscosity was 100 mPa·s; (**e**) the variation of the total resistance force with the pump displacement and the drilling fluid viscosity when the diameter of overflow hole 1 and the drilling fluid density were 7 mm and 1300 kg/m^3, respectively.

the overflow hole 1 greatly decreases the total resistance. The total resistance of the inner tube decreases by 80% to only 3.29 kN with the diameter of the overflow hole 1 increasing from 4 to 7 mm (the triggering pump displacement and the drilling fluid density are 10 L/s and 1300 kg/m^3, respectively). (3) The total resistance increases remarkably with the increase of the triggering pump displacement during the inner tube lifting process. When the triggering pump displacement increases from 10 to 30 L/s at the overflow hole diameter of 7 mm and the drilling fluid density of 1300 kg/m^3, the total resistance of the inner tube increases to 8.36 times the former. This means that smaller pump displacement in the inner tube lifting process is conducive to improving the success rate of the in-situ pressure sealing due to the smaller total resistance. However, in the oil and gas drilling site, the pump displacement in the drilling process can generally reach 30 L/s. The sudden decrease to less than 10 L/s in the inner tube lifting process places greater demands on the working capacity of the pump group. Therefore, to improve the applicability of coring tools for the site, it is expected that the lifting of the inner tube can be effectively conducted under the pump displacement of 20 L/s. This means that the total resistance should remain lower than the maximum total shear force of the three pins F_{she} under the pump displacement of 20 L/s. Thus, from Fig. 5(d), this requirement can be met when the diameter of the overflow hole 1 exceeds 7 mm, in the working environment where the drilling fluid density is less than 1700 kg/m^3. On the other hand, Fig. 5(e) shows the variation of the total resistance force with the pump displacement and the drilling fluid viscosity when the diameter of overflow hole 1 and the drilling fluid density were 7 mm and 1300 kg/m^3, respectively. It can be seen that the effect of drilling fluid viscosity on the total resistance F_R is minimal and can be practically neglected. For example, at a pump displacement of 30 L/s, increasing the drilling fluid viscosity from 50 to 200 mPa·s results in a change in total resistance from 27.511 to 27.514 kN, an increase of less than 0.01%.

In summary, the total resistance of the inner tube can be greatly reduced by increasing the diameter of the overflow hole 1 of the inner tube, but an increase in drilling fluid density will also lead to higher resistance in the inner tube. On the other hand, the effect of drilling fluid viscosity on the total resistance F_R is minimal and can be practically neglected. Therefore, when pressure coring is performed in layers that require the circulation of drilling fluid with higher density, it may be necessary to further adjust the structure of the pressure sealing subsystem to increase the success rate of in-situ pressure sealing in the downhole. In addition, when the diameter of the overflow hole 1 exceeds 7 mm, the total resistance is still less than the maximum total shear force of the three pins F_{she} under the pump displacement of 20 L/s, in the working environment where the drilling fluid density is less than 1700 kg/m^3. In other words, in this condition, the inner tube can be effectively lifted.

2.3. Flow field analysis

Theoretical calculations in Section 2.2 suggest that increasing the diameter of overflow hole 1 of the inner tube is conducive to decreasing the total resistance of the inner tube and further increasing the success rate of in-situ pressure sealing. However, during core drilling, the diameter of the overflow hole in the inner tube will affect the circulation flow of drilling fluid. An unreasonable hydraulic structure may lead to uncertainty regarding the service performance of the pressure sealing subsystem. Therefore, in this section, CFD simulations are used to explore the flow characteristics inside the pressure sealing subsystem and further determine the structure parameter of the pressure sealing subsystem.

2.3.1. Numerical model

The overflow hole 1, with a diameter of 7 mm, is preliminarily selected as the structural parameter of the pressure sealing system, and CFD simulations are carried out. In deep oil and gas exploration, the high drilling fluid displacement leads to a considerable flow velocity within the pressure sealing subsystem, typically causing turbulent flow conditions. Consequently, the standard k-ε model is used in this paper to describe the flow characteristics, and the fluid is defined as Newtonian fluid and incompressible. The 3D model of the pressure sealing system, the flow computational domain established according to the structure of the pressure sealing system, and the boundary conditions are shown in Fig. 6. Drilling fluids typically have densities in the range of 1000–2000 kg/m^3 in the onshore oil and gas drilling (Al-Shargabi et al., 2024; Gao, 2024), depending on well depth, pressure conditions, and formation requirements (Radich et al., 2023). Therefore, the liquid phase in this simulation is the drilling fluid with densities of 1300, 1500, and 1700 kg/m^3, along with a viscosity of 100 mPa·s. The inlet boundary condition is defined as a "velocity inlet" of 4.9, 3.3, and 1.63 m/s, which is converted from the pump displacement of 30, 20, and 10 L/s. The outlet boundary condition is specified as a "pressure outlet" set at 30 MPa, which is estimated according to the well depth of 2000–3000 m. The wall boundary is set as "no slip".

The computational domain is meshed using a sweep algorithm to generate hexahedral grids with higher calculation accuracy. Local mesh refinement is applied near the overflow holes, where significant velocity and pressure variations occur. In other regions, a relatively coarser grid is used to reduce the number of grids and save calculation time. In addition, a mesh independence study is conducted to increase the accuracy of the simulation results. To assess mesh independence, the maximum velocity within the computational domain is analyzed under an inlet velocity of 4.9 m/s using different mesh numbers. The calculated results are shown in Fig. 7, when the mesh number reaches approximately 1,681,695, the maximum velocity in the domain converges to about 10.9 m/s. Thus, the solution can be identified as mesh independence. Therefore, to save computing resources, the mesh number of 1,681,695 is selected for this simulation.

2.3.2. Simulation results

Fig. 8 shows the velocity streamlines within the pressure sealing subsystem under specific inlet velocities and fluid densities. It is observed that (1) the two chambers of the pressure sealing subsystem are intentionally separated, and connected only through overflow holes 1 and 2. The drilling fluid enters the outer chamber through overflow hole 2 and exits via overflow hole 1. (2) Due to the velocity difference between the two chambers, a distinct vortex region forms near the overflow hole 2 in the outer chamber, and its area expands as the inlet velocity (pump displacement) increases. (3) The maximum velocity in the subsystem occurs at the overflow hole 2. And it rises to 3.7 times when the inlet velocity rises from 1.63 to 4.9 m/s (4) From Fig. 8(b), the fluid density has a minimal impact on the overall velocity field

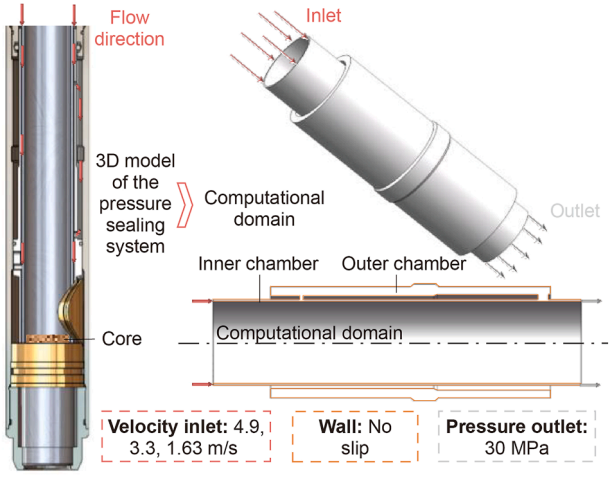

Fig. 6. 3D model of the pressure sealing system, computational domain, and the boundary conditions.

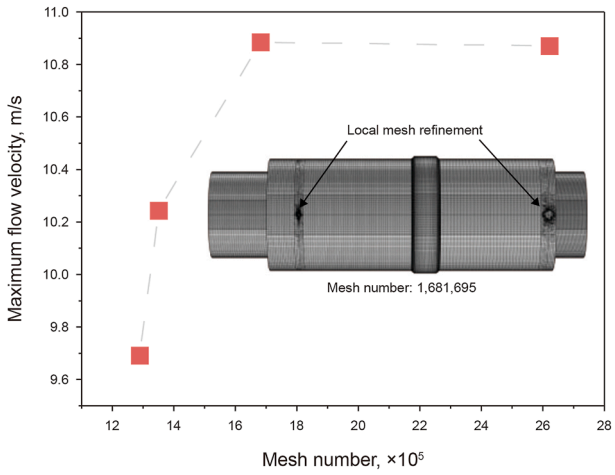

Fig. 7. Relationship between the maximum flow velocity with the mesh number. The inside illustrations show the established mesh domain.

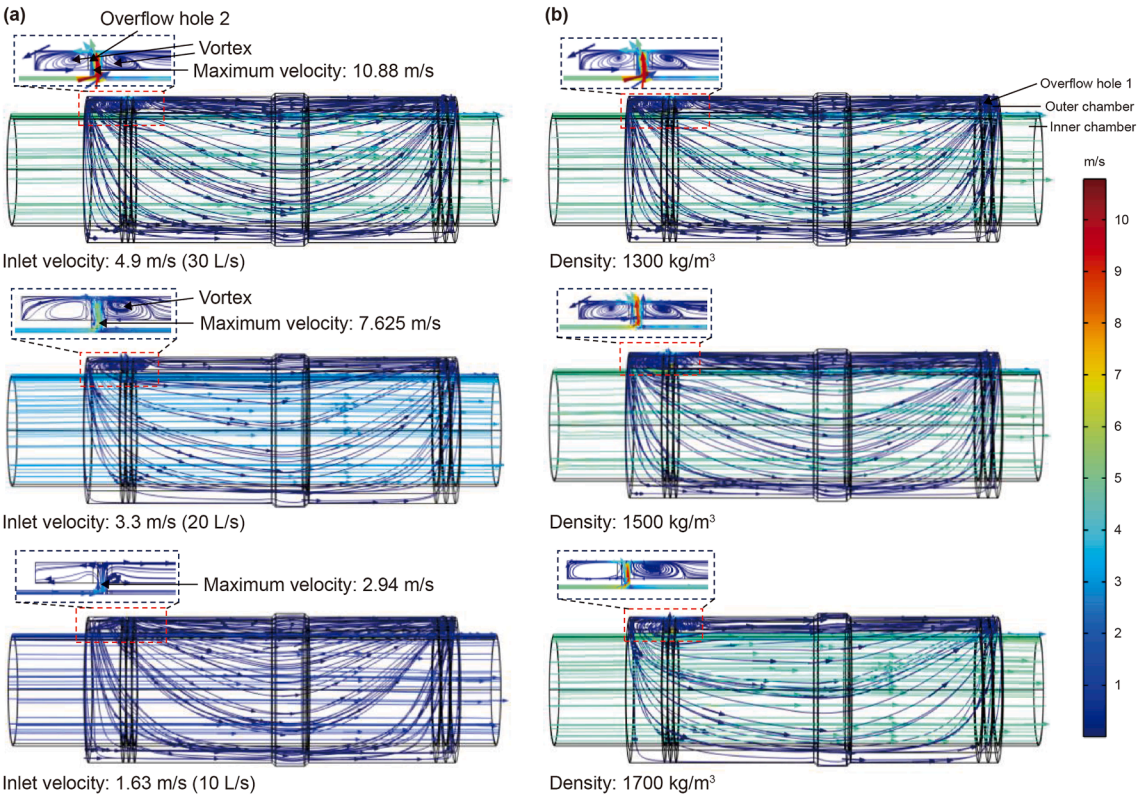

Fig. 8. Velocity streamlines within the pressure sealing subsystem under specific (**a**) inlet velocities (fluid density: 1300 kg/m^3) and (**b**) fluid densities (inlet velocity: 4.9 m/s).

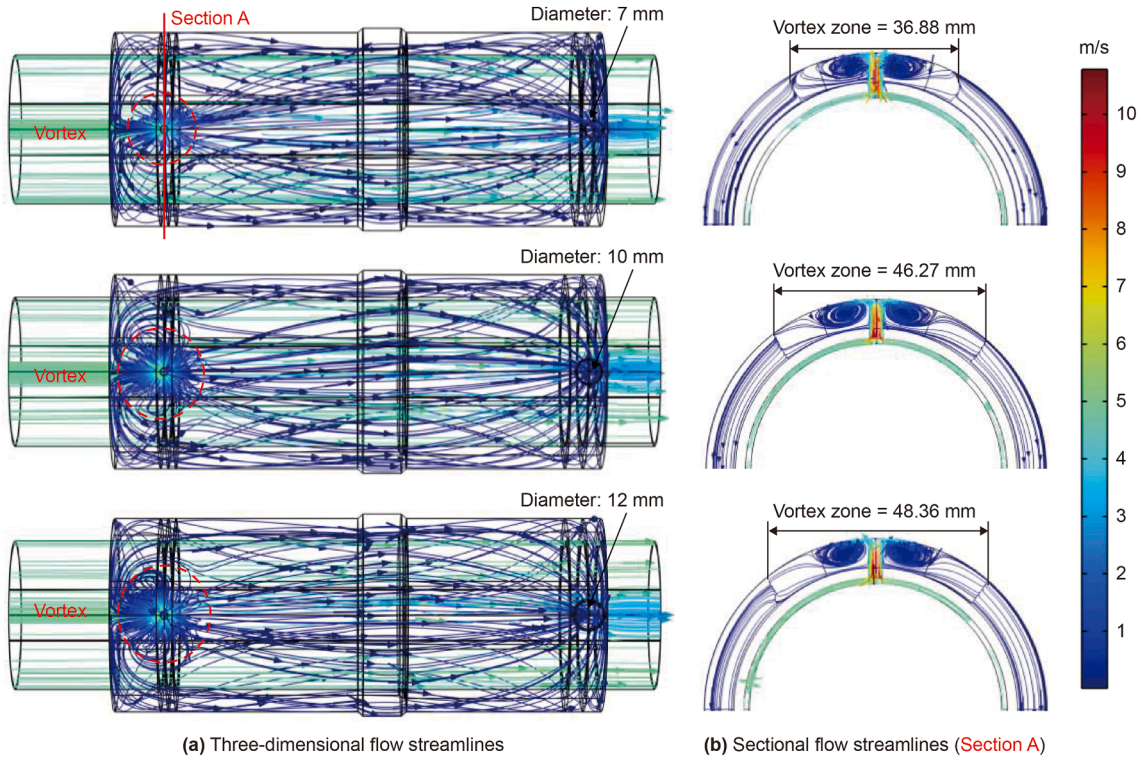

Fig. 9. Velocity streamlines in the pressure sealing subsystem with different diameters of the overflow hole 1 (inlet velocity: 4.9 m/s, fluid density: 1300 kg/m^3).

distribution in the computational domain. However, a higher density significantly enlarges the vortex area near overflow hole 2.

Velocity streamlines in the pressure sealing subsystem with different overflow hole 1 diameter are shown in Fig. 9. From Fig. 9(a), the overflow hole 1 diameter has minimal impact on the drilling fluid velocity in the pressure sealing subsystem. However, it is worth noting that the vortex area near overflow hole 2 gradually increases with the diameter of overflow hole 1. To quantitatively describe the size of the vortex zone, sectional flow streamlines in Section A are extracted, as shown in Fig. 9(b). As the diameter of the overflow hole 1 increases from 7 to 12 mm, the width of the vortex zone increases by 24%, from 36.88 to 48.26 mm. Unfortunately, vortex and backflow are generally undesirable (Zheng et al., 2015), as they hinder particle discharge from overflow hole 1, increasing particle accumulation in the outer chamber and potentially compromising the sealing success rate after coring. Therefore, although increasing the diameter of the overflow hole 1 of the inner tube is beneficial to reduce the resistance of the inner tube during the upward process, it also increases the vortex area in the outer chamber of the pressure sealing subsystem during drilling, increasing the uncertainty of the sealing process. To enhance the reliability of pressure sealing, overflow hole 1 diameter should be minimized while ensuring sufficient lifting resistance. Thus, the moderate diameter of the overflow hole 1 of 7 mm is considered the most reasonable.

3. Numerical and laboratory research on the service performance

3.1. Numerical verification for the working performance

Primarily due to the presence of solid-phase particles in the wellbore fluid, which settle on the sealing surface and the assembly space of the component during the coring process, making it difficult for the IPP-coring system to preserve the in-situ pressure reliably. A dynamic sealing structure within the inner tube and the pressure bearing tube, and a close-fitting structure of the sealing face of the pressure controller with the bottom of the inner tube, were designed in the pressure sealing subsystem to overcome this inherent problem. Given the complexity and inaccessibility of the downhole environment, along with the high cost and difficulty of experimental quantitative evaluation, numerical verification is first conducted in this section to demonstrate the superiority of the novel structure.

3.1.1. Numerical model

The liquid-solid two-phase flow characteristics in the novel and original pressure sealing subsystems are described using the two-way coupled Euler-Lagrange method. The motion equation of solid particles is available in (Feng et al., 2022). The circulating drilling fluid is treated as a homogeneous, incompressible Newton fluid. The interactions between solid particles, such as collision, bonding, and fragmentation, are not considered and solid particles are assumed spherical. The volume fraction of solid particles within the circulated drilling fluid does not exceed 10%.

Our goal in this section is to comprehend how solid particles settle on the pressure sealing subsystem as well as verify the superiority of the novel structure. For this reason, the novel structure with the moderate diameter of the overflow hole 1 of 7 mm which is considered the most reasonable in the last section is used to compare with the original structure, the cross-sectional structure of the original and novel structure is shown in Fig. 10. The inlet releases the solid particles with the same initial velocity with the

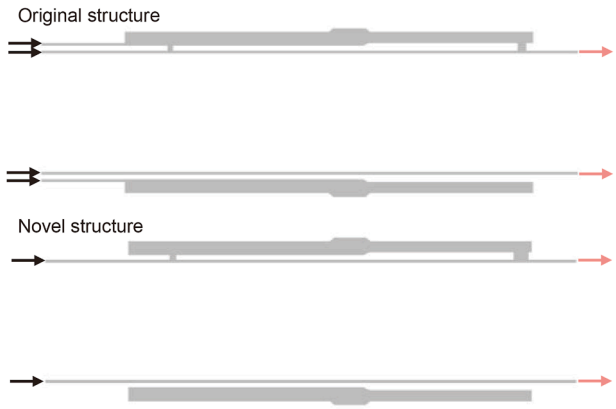

Fig. 10. Cross-sectional structure of the original and novel structure.

fluid. When the flow velocity of the fluid near the particle impact point (the distance is one diameter length of the particle along the wall-normal) is below a threshold value of 0.1 m/s in this study, the particle is considered settled on the wall under the local flow pressure. Since the threshold velocity utilized in this work is suggested by the pertinent literature (Chen, 2016; Liu et al., 2011) and our experience, we must state that they are dubious. Because of the challenging conditions, it is difficult to estimate the precise values from the experiment. However, the assumptions are helpful to better understand the settlement of the particles and bring the solid particle motion simulation closer to reality.

The simulation parameters are set as compatible with subsequent laboratory downhole circulation and drilling tests (Section 3.2). Therefore, the liquid phase in this numerical model has a density of 1100 kg/m^3 and a viscosity of 30 mPa·s. The solid phase consisted of inertia particles, which have a density and diameter of 2650 kg/m^3 and 0.3 mm, respectively. The particles enter the calculation domain at a constant velocity assumed the same as the liquid phase of 1.36 m/s. It is conversed from the pump displacement of 500 L/min. The outlet is set as a “pressure outlet”, and the outlet static pressure of 0.2 MPa is estimated according to the depth of the laboratory experimental well. Further, steady calculations with an iteration of 5000 were conducted to obtain the particle motion behaviors.

3.1.2. Results of the numerical verification

Fig. 11 shows the particle motion trajectories and the settled particle distributions on the walls of the original and novel structures. From Fig. 11(a) and (b), in the original structure, particles first enter the outer chamber of the pressure sealing subsystem, then pass through overflow holes 1 and 2 into the inner chamber, and finally exit the subsystem. In contrast, for the novel structure, particles enter the outer chamber from overflow hole 2 and exit from overflow hole 1. Compared to the original structure, the particle trajectory in the outer chamber is significantly sparser, which means that the number of particles invading the outer chamber of the pressure sealing subsystem is significantly reduced after optimization. From Fig. 11(c) and (d), the settled particles in the original structure dispersed on the inner and outer walls of the outer chamber, while after optimization, only a certain number of particles settled on the top of the outer chamber. Further, the settlement ratio of the particles on the wall of the original and novel structure is calculated, as shown in Fig. 12. The settlement ratio of particles in the novel structure is only 32% of that of the original one. It demonstrates that the novel structure significantly reduces the accumulation and adhesion of particles, and it is expected to improve the reliability of the device.

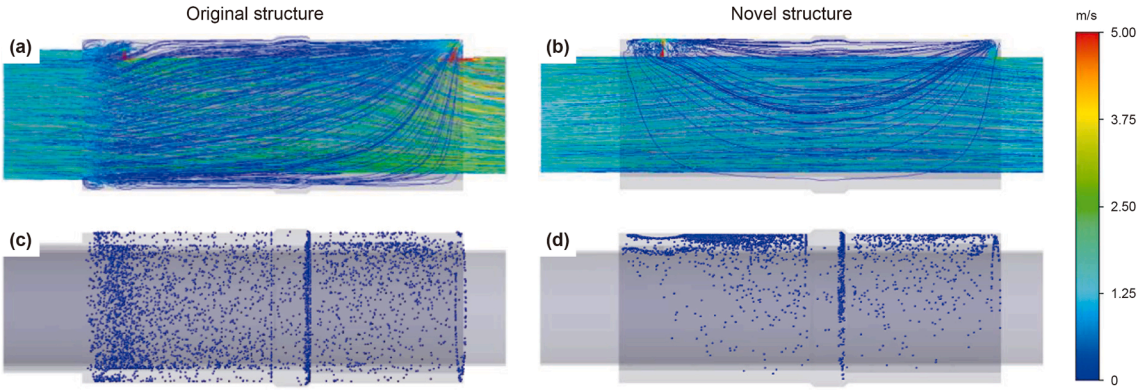

Fig. 11. (**a**, **b**) Particle motion trajectories and (**c**, **d**) the settled particle distributions on the walls of the original and novel structures.

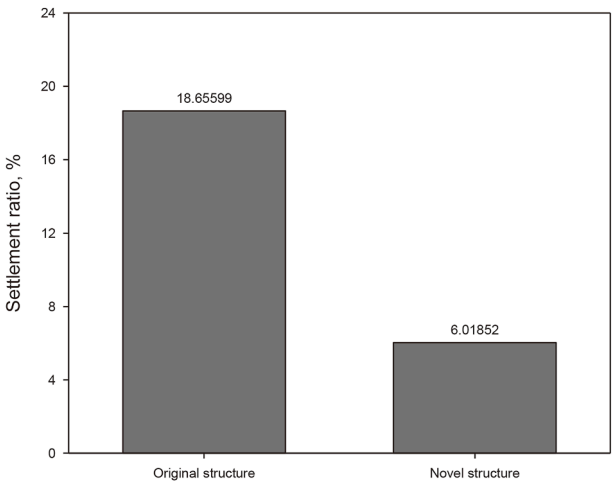

Fig. 12. Particle settlement ratio in the original structure and novel structure, respectively.

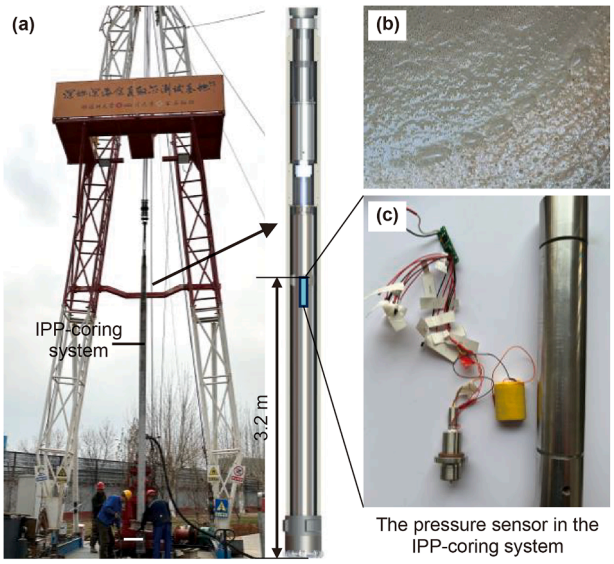

Fig. 13. Details of the laboratory downhole circulation and drilling tests: (**a**) the downhole circulation and drilling test platform with depth of about 13 m after filling in the cement, the IPP-coring system was ready to be lowered into the hole; (**b**) the bentonite-based drilling fluid with the density and funnel viscosity of 1.1 g/cm^3 and 60 s, respectively; (**c**) the pressure sensor used to verify the sealing performance of the pressure sealing subsystem in the downhole environment with drilling fluid.

3.2. Laboratory downhole circulation and drilling tests

By theoretical analysis and CFD simulation, the fundamental structural parameters of the pressure sealing subsystem were determined. Subsequently, a prototype of the pressure sealing subsystem was manufactured and incorporated into the IPP-coring system. Furthermore, laboratory downhole circulation and drilling tests were performed to evaluate the sealing performance of the pressure sealing subsystem in a drilling fluid environment.

3.2.1. Test methods

Laboratory downhole circulation and drilling tests were conducted on the drilling platform shown in Fig. 13(a). This platform is equipped with a DWB-850/4-75 mud pump (China Geological Equipment Group Co., Ltd) and an XY-5 drilling rig (China Geological Equipment Group Co., Ltd). The depth of the hole is about 13 m after filling in the cement. The tests use a bentonite-based drilling fluid with a density and funnel viscosity of 1100 kg/m^3 and 60 s, respectively, as shown in Fig. 13(b). In addition, as shown in Fig. 13(c), a self-developed pressure sensor with a 1 MPa measuring range is installed in the IPP-coring system to assess the sealing performance of the pressure sealing subsystem under downhole drilling fluid conditions. The sensor is positioned approximately 3.2 m from the drill bit bottom.

The test process is as follows: First, the pressure sealing subsystem designed in this study was integrated into the IPP-coring system and then lowered into the bottom of the hole. Subsequently, drilling fluid was circulated in the IPP-coring system for 50 min at a displacement of 500 L/min before the core drilling process. This step aimed to account for the impact of drilling fluid on the pressure sealing subsystem during the down trip process in real field conditions, and the circulation pump pressure is about 0.1 MPa. Then, the pump was turned off to keep the IPP-coring system in the downhole environment for 70 min. Afterward, the core drilling was conducted at a displacement of 500 L/min under the power provided by the drilling rig, with a total footage of 1 m. Next, the drilling assembly at the bottom of the hole was raised 1 m to detach the threaded joint, and a ball drop operation was conducted. Subsequently, the sequences of mechanical actions were triggered under the pump displacement of 500 L/min to realize the downhole pressure sealing. Finally, the pressure core was recovered to the surface. The laboratory test parameters are summarized in Table 1.

3.2.2. Test results

The results of the laboratory downhole circulation and drilling tests are shown in Fig. 14. From Fig. 14(a), there are fewer sand

Table 1
Laboratory test parameters.

Parameters	Values
Density of the drilling fluid, kg/m^3	1100
Funnel viscosity of the drilling fluid, s	60
RPM, r/min	166
Displacement, L/min	500
Accumulated footage, m	1
Pump pressure (before ball drop), MPa	≈0.1
Pump pressure (after ball drop), MPa	≈1
Coring weight, kN	≈9.8

Table 2
Properties of the brine-base drilling fluid.

Density, g/cm^3	Funnel viscosity, s	pH	Filter loss, mL
1.32	52	9	3.2

particles settled in the outer surface of the inner tube of the novel structure in this study compared with that of the original structure. This may indicate a reduction in particle accumulation within the annulus between the inner and outer tubes (outer chamber) for the optimized pressure sealing subsystem. The pressure variation curve is shown in Fig. 14(b). When pumping circulation or drilling commenced, the sensor recorded pressure values approximately 0.08 MPa higher than those during the standing and surface treatment stages, reaching approximately 0.28 MPa. This increase is attributed to hydrodynamic pressure generated by the drilling fluid flow. During the surface treatment stage, the IPP-coring system maintained an internal pressure of 0.2 MPa for approximately 90 min, this pressure of 0.2 MPa is considered as in-situ pressure due to the sensor being approximately 9–10 m at the bottom of the hole with the drilling fluid of 1.1 g/cm^3 when the pressure sealing action was achieved. In addition, as shown in Fig. 14(c), a core sample measuring 0.9 m in length was successfully obtained during the drilling process. Overall, these results confirm that the pressure sealing subsystem designed in this study effectively achieves in-situ pressure sealing in a downhole drilling fluid environment.

4. Field application

In the laboratory downhole circulation and drilling tests, the pressure sealing subsystem designed in this study effectively achieved in-situ pressure sealing. However, the real field conditions are more complex. Therefore, the performance of the pressure sealing subsystem was further verified by real field tests for onshore oil and gas explorations.

4.1. Field application background and process

The field application was carried out in a development well in the Hubei Province, China. The well has an 8 1/2″ diameter and a designed depth of 2061 m, with an inclination angle of less than 30°. The target layer, comprising gray-green mudstone with siltstone, is located at a depth of 1970 m, with designed coring footage

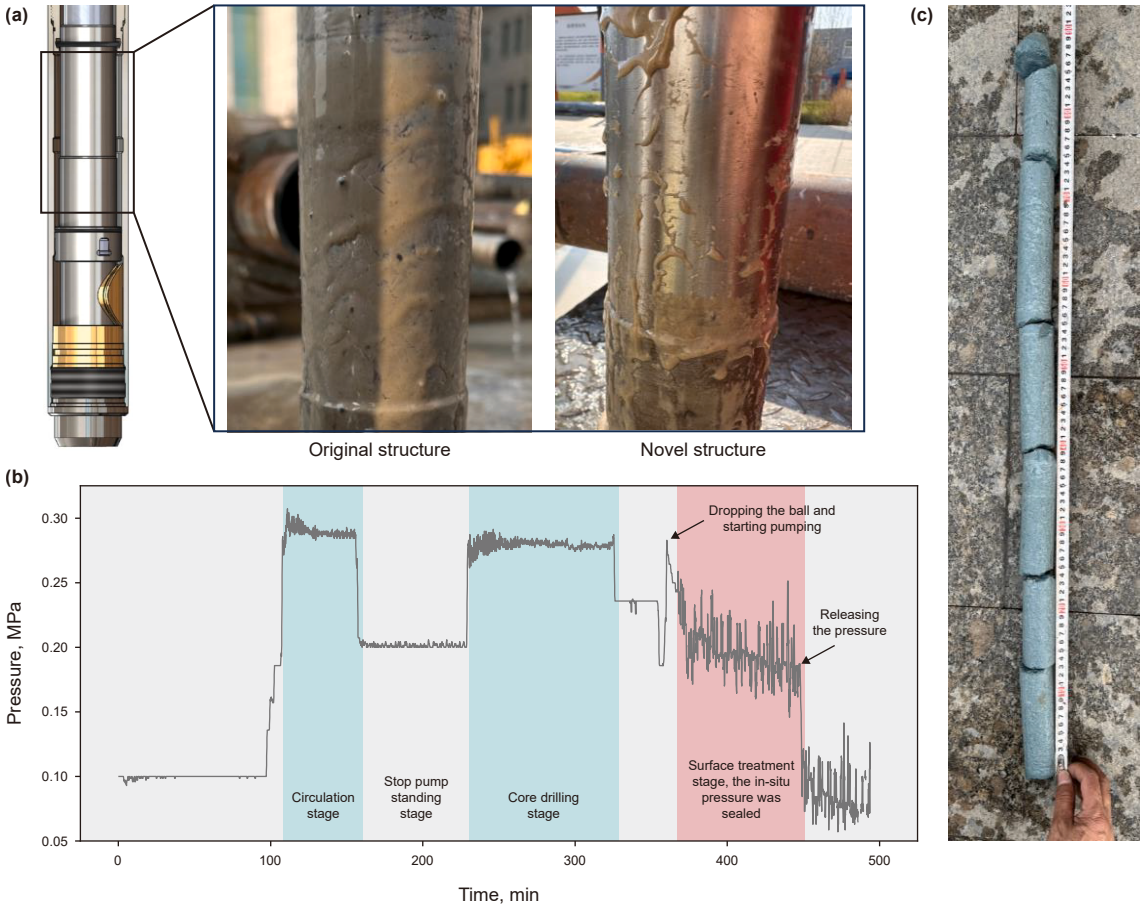

Fig. 14. Results of the laboratory downhole circulation and drilling tests: (**a**) the photos of the inner tube after the tests; (**b**) the pressure variation curve in the IPP-coring system, the curve was obtained by filtering the data collected by the sensor; (**c**) the obtained core sample by the IPP-coring system with the pressure sealing subsystem.

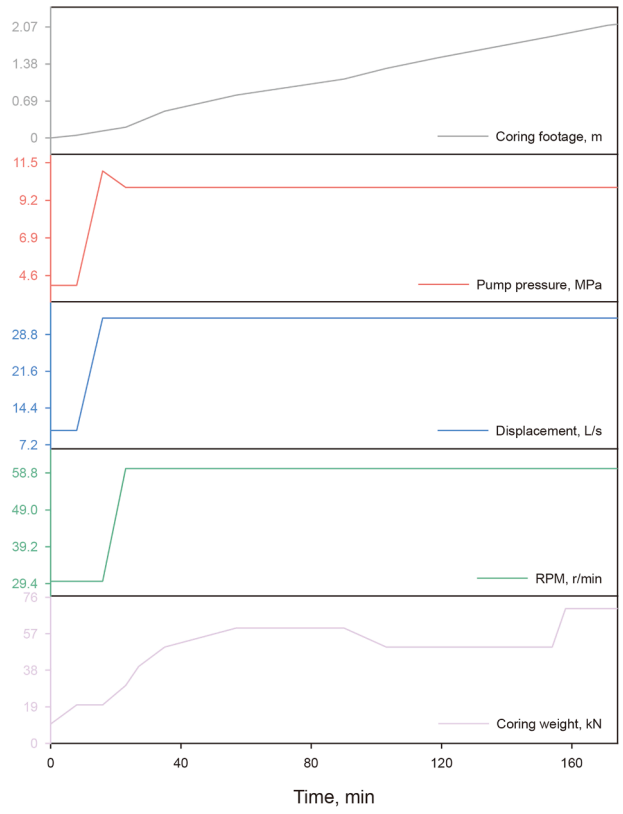

Fig. 15. Parameter curves in core drilling.

of 2.1 m. The pressure coring was carried out using a brine-base drilling fluid, with its properties detailed in Table 2.

Before the core drilling, the wellbore underwent a cleaning process using drilling fluid for 1–2 rounds to minimize bottom grit. Following this, the bottom hole assembly, comprising 18 extra-weight drill pipes and the IPP-coring system, was lowered into the hole to conduct the core drilling process, facilitated by the torque provided by the rotary table in the wellhead. After that, the drill string was lifted to cut the core, and the ball drop operation was conducted. Upon activation by the steel ball, a series of mechanical actions were carried out in the pressure sealing subsystem to achieve in-situ pressure sealing. The completion of these actions was confirmed by the increase in the circulating pressure of the drilling fluid following the ball drop operation. Afterward, the IPP-coring system was recovered through the conventional trip. For a more comprehensive understanding of the pressure coring principle and process of the IPP-coring system, please refer to (Guo et al., 2024).

Fig. 15 shows the parameters of the core drilling process. The RPM of the IPP-coring system is set at about 60 r/min. In addition, the drilling fluid is pumped at the displacement of 32 L/s, resulting in the 10 MPa pressure loss along the drilling string. According to the real-time drilling conditions, the coring rate is controlled by adjusting the coring weight, and the average footage efficiency is about 0.72 m/h (excluding the core grinding process). After core drilling, the drilling string was slowly lifted to cut the core. Then, the ball drop operation was conducted, after which the pump was started at a flow rate of 10 L/s and gradually increased to 20 L/s. During this operation, the pump pressure rose to 1.75 times the original circulation pressure, indicating that the series of mechanical actions in the IPP-coring system had been completed.

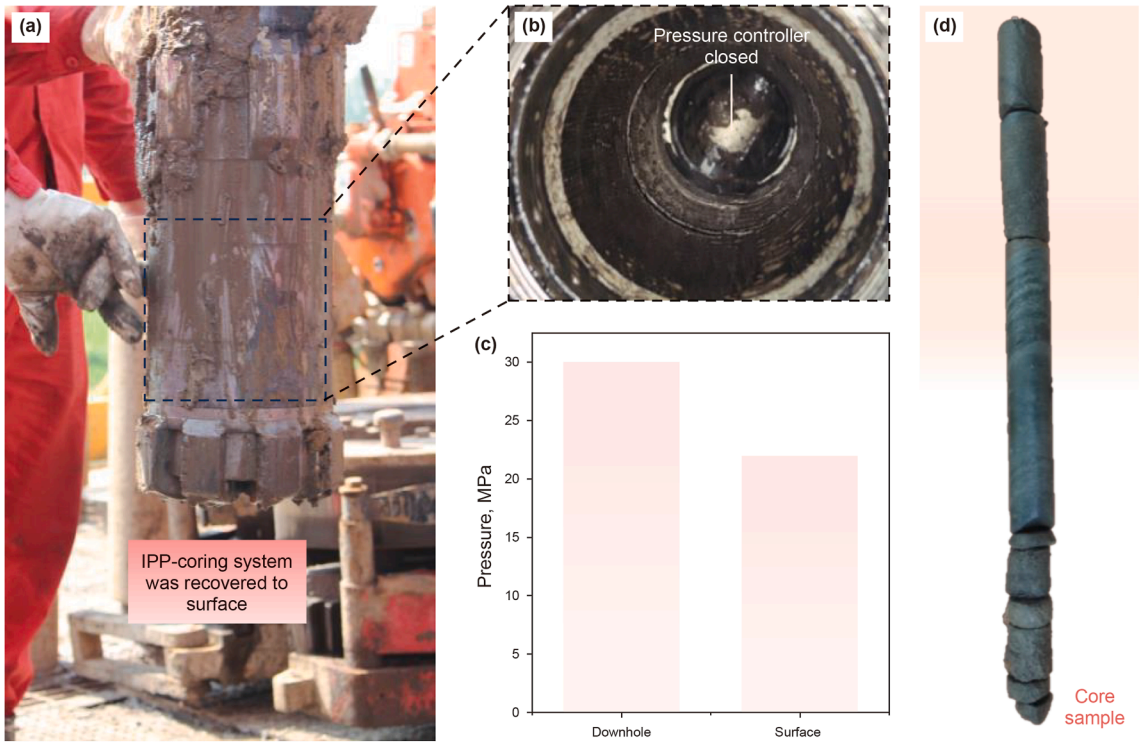

Fig. 16. Field application results: (**a**) photograph shows the IPP-coring system was recovered from the downhole; (**b**) pressure controller in the pressure sealing subsystem successfully closed; (**c**) pressure value shows the comparation of the actual pressure at the bottom to the pressure sealed by the IPP-coring system after it is recovered to surface; (**d**) photograph shows the obtained core sample.

4.2. Field application results

Field application results are shown in Fig. 16. From Fig. 16(a) and (b), when the IPP-coring system was recovered, the pressure controller in the pressure sealing subsystem was successfully closed. This means a series of mechanical actions was completed successfully in the downhole environment. Fig. 16(c) shows the comparison of the downhole pressure to the pressure sealed by the IPP-coring system after it is recovered to the surface. The sealed pressure is about 22 MPa, which is about 73.3% of the in-situ pressure. Although there is a slight decrease in the surface pressure compared with the downhole pressure due to the unavoidable changes in temperature and volume of the IPP-coring system under high pressure, the sealing performance of the pressure sealing subsystem can be effectively proved. Notably, maintaining full in-situ pressure is extremely difficult because the decrease in surface temperature relative to bottom temperature will inevitably lead to a drop in pressure. In addition, Fig. 16(d) shows the photo of the obtained core sample, the core sample with 50 mm in diameter and 1.95 m in length was obtained at 1970 m, and the recovery rate is 82%. The field test proves that the pressure sealing subsystem can effectively complete the in-situ pressure sealing. In addition, the coring performance of the IPP-coring system was successfully verified.

5. Limitations and future work

There are several limitations in this work that future studies can further explore. First, the current work primarily focuses on the design of a novel pressure sealing subsystem, with its service performance verified through numerical simulation, laboratory test, and field coring operation. These simulations showed that the particle settlement ratio in the novel structure is only 32% of that in the original design. Although these results are promising, more extensive experimental studies, especially under conditions rich in particles, are necessary. Second, although initial laboratory tests and field applications have preliminarily validated the performance of the novel pressure sealing subsystem, quantitative experimental studies in drilling environments with high concentrations of rock particles are still lacking. Third, there have been relatively few pressure coring operations conducted in actual oil and gas drilling sites. As a result, more field operations are needed, especially at depths exceeding 2000 m, to fully verify the effectiveness and success rate of the pressure sealing subsystem in the real fields.

To address these limitations, future research can further explore: (1) Quantitative and visualized experiments: Future studies will explore more advanced, quantitative experimental methods to investigate the settlement and adhesion behavior of particles at critical sealing areas in the pressure sealing subsystem, especially in environments rich in particles. (2) Further optimization of hydraulic structure: Another key area of future research will involve further optimizing the hydraulic structure of the pressure sealing subsystem to enhance its reliability, particularly in increasingly deep and complex service environments. This will require considering the adverse effects of particles during pressure coring operations. (3) Field validation and application expansion: Continued field testing will be crucial, especially in diverse geological conditions, to ensure service performance and reliability across different environments. Additionally, there is potential to extend the application of this method beyond oil and gas exploration to other industries facing similar challenges, such as geothermal energy extraction or mining. On the other hand, in future work, we will extend the application of the tool to exploration wells and systematically conduct physical property testing on the obtained cores. These efforts will allow us to more thoroughly verify the advantages of pressure core sampling in preserving reservoir characteristics and provide stronger support for its engineering application.

6. Conclusion

In this paper, a novel pressure sealing subsystem was designed. The theoretical calculation and CFD simulation were used to determine the key structure parameters of the pressure sealing subsystem, and the sealing performance in the downhole environment of the subsystem was verified by laboratory tests and field application. The following conclusions are drawn:

(1) To enhance the reliability of pressure sealing in the real downhole environment, a dynamic sealing structure within the inner tube and the pressure bearing tube and the close-fitting structure of the sealing face of the pressure controller with the bottom of the inner tube was designed for the pressure sealing subsystem. The in-situ pressure sealing is achieved by the successful lifting of the inner tube and the closing of the pressure controller in the pressure sealing subsystem.

(2) During the inner tube lifting process, the smaller pump displacement in the inner tube lifting process and the larger diameter of the overflow hole are conducive to decreasing the lifting resistance of the inner tube. With the diameter of overflow hole 1 increasing from 4 to 7 mm at the triggering pump displacement of 10 L/s and the drilling fluid density of 1300 kg/m^3, the total resistance of the inner tube decreases by 80%. When the triggering pump displacement increases from 10 to 30 L/s at the diameter of the overflow hole 1 of 7 mm and the drilling fluid density of 1300 kg/m^3, the total resistance of the inner tube increases to 8.36 times the previous value.

(3) CFD simulations indicate that a harmful vortex is formed near the overflow hole 2. As the diameter of overflow hole 1 increases from 7 to 12 mm, the width of the vortex zone increases by 24%, from 36.88 to 48.26 mm. To reduce the harmful vortex, a smaller diameter for overflow hole 1 should be selected, provided it satisfies the lifting resistance, with a moderate diameter of 7 mm considered most reasonable.

(4) Numerical verification shows that the particle settlement ratio in the novel structure is only 32% of that in the original design. Laboratory tests demonstrate that the pressure sealing subsystem successfully sealed the in-situ pressure of 0.2 MPa at a depth of approximately 9–10 m (the drilling fluid density is 1.1 g/cm^3). Field application results indicate that an in-situ core sample of 1.95 m was obtained at 22 MPa from a depth of about 1970 m. Those results demonstrate the superiority and sealing performance of the pressure sealing subsystem in the downhole environment.

(5) The novel pressure sealing subsystem not only has twice the pressure-preserved capacity of the current state-of-the-art pressure coring tool (PCS, 70 MPa), but also may have higher engineering reliability and pressure retention coring success rate. These advantages will be further verified through additional field trials in future studies.

CRediT authorship contribution statement

Da Guo: Writing – original draft, Visualization, Validation, Software, Methodology, Investigation, Funding acquisition, Formal analysis, Data curation, Conceptualization. **Ling Chen:** Methodology, Investigation, Data curation, Conceptualization. **Jia-Nan Li:**

Methodology, Investigation, Conceptualization. **Le Zhao:** Methodology, Investigation. **Yi-Wei Zhang:** Methodology, Investigation. **Ding-Ming Wang:** Methodology, Investigation. **Xin Fang:** Methodology, Investigation. **Zhi-Qiang He:** Methodology, Investigation, Funding acquisition. **Lin Dai:** Methodology, Investigation. **He-Ping Xie:** Writing – review & editing, Supervision, Project administration, Methodology, Investigation, Conceptualization.

Declaration of competing interest

The authors declare that they have no known competing financial interests or personal relationships that could have appeared to influence the work reported in this paper.

Acknowledgments

The authors are grateful for the financial support from the National Natural Science Foundation of China (No. 523B2037), Sichuan Province Innovative Talent Funding Project for Postdoctoral Fellows, and Sichuan Science and Technology Program (No. 2023NSFSC0790).

References

Abegg, F., Hohnberg, H.J., Pape, T., et al., 2008. Development and application of pressure-core-sampling systems for the investigation of gas-and gas-hydrate-bearing sediments. Deep Sea Res. Oceanogr. Res. Pap. 55 (11), 1590–1599. https://doi.org/10.1016/j.dsr.2008.06.006.

Al-Ghathian, F., Tarawneh, F., Musfag, S., 2005. Friction forces in O-ring sealing. Am. J. Appl. Sci. 2 (3), 626–632. https://doi.org/10.3844/ajassp.2005.626.632.

Al-Shargabi, M., Davoodi, S., Wood, D.A., et al., 2024. Hole-cleaning performance in non-vertical wellbores: a review of influences, models, drilling fluid types, and real-time applications. Geoenergy Sci. Eng. 233, 212551. https://doi.org/10.1016/j.geoen.2023.212551.

Ashena, R., Thonhauser, G., 2018. Coring Methods and Systems. Springer, pp. 1–243. https://doi.org/10.1007/978-3-319-77733-7.

Chen, X., 2016. Research on Adhesion Mechanism of Shaly Cuttings and Hydraulic Optimization Design of PDC Bits. PhD Dissertation. China University of Petroleum, East China.

Dickens, G.R., Paull, C.K., Wallace, P., et al., 1997. Direct measurement of *in situ* methane quantities in a large gas-hydrate reservoir. Nature 385 (6615), 427–428. https://doi.org/10.1038/385426a0.

Dickens, G.R., Schroeder, D., Hinrichs, K.U., 2003. The pressure core sampler (PCS) on ODP leg 201: general operations and gas release. In: Proc. Ocean Drill. Program.. https://doi.org/10.2973/ODP.PROC.IR.201.103.2003.

Feng, C., Liu, W., Gao, D., 2022. CFD simulation and optimization of slurry erosion of PDC bits. Powder Technol. 408, 117658. https://doi.org/10.1016/j.powtec.2022.117658.

Gao, C.H., 2024. Drilling fluids for shale fields: case studies and lessons learnt. Unconvent. Resourc. 4, 100070. https://doi.org/10.1016/j.uncres.2023.100070.

Guo, D., Xie, H., Chen, L., et al., 2023a. In-situ pressure-preserved coring for deep exploration: insight into the rotation behavior of the valve cover of a pressure controller. Pet. Sci. 20 (4), 2386–2398. https://doi.org/10.1016/j.petsci.2023.02.020.

Guo, D., Chen, L., Zhou, Z., et al., 2023b. Development of a pressure coring system for the investigation of deep underground exploration. Int. J. Min. Sci. Technol. 11 (33), 1351–1364. https://doi.org/10.1016/j.ijmst.2023.10.001.

Guo, D., Xie, H., Gao, M., et al., 2024. In-situ pressure-preserved coring for deep oil and gas exploration: design scheme for a coring tool and research on the in-situ pressure-preserving mechanism. Energy 286, 129519. https://doi.org/10.1016/j.energy.2023.129519.

Hu, Y., Xie, J., Xue, S., et al., 2022. Research and application of thermal insulation effect of natural gas hydrate freezing corer based on the wireline-coring principle. Pet. Sci. 19 (3), 1291–1304. https://doi.org/10.1016/j.petsci.2021.11.019.

Huang, W., Chen, L., Li, J., et al., 2023. R&D and experimental research of pressure-preserved triggering device for horizontal pressure-preserved coring in coal mines. Coal Geol. Explor. 51 (8), 39–46. https://doi.org/10.12363/issn.1001-1986.22.12.0933.

Jackson, K., Witte, U., Chalmers, S., et al., 2017. A system for retrieval and incubation of benthic sediment cores at *in situ* ambient pressure and under controlled or manipulated environmental conditions. J. Atmos. Ocean. Technol. 34 (5), 983–1000. https://doi.org/10.1175/JTECH-D-16-0248.1.

Kawasaki, M., Umezu, S., Yasuda, M., 2006. Pressure temperature core Sampler (PTCS). J. Jpn. Assoc. Pet. Technol. 1 (71), 139–147. https://doi.org/10.3720/japt.71.139.

Kleinstreuer, C., 2018. Modern fluid dynamics. CRC Press, Boca Raton, FL, USA.

Kumar, B.K., Reddy, M.V.R., Kumar, K., 2015. Pin shear–material testing and validation using finite element analysis (ANSYS). Int. J. Eng. Res. Technol. 4, 165–170. https://doi.org/10.17577/ijertv4is070151fatcat:vtfby7bsovavficobt3yvgswti.

Kundu, P.K., Cohen, I.M., Dowling, D.R., 2015. Fluid Mechanics. Academic Press.

Kvenvolden, K.A., Barnard, L.A., Cameron, D.H., 1983. Pressure core barrel: application to the study of gas hydrates, deep sea drilling project site 533, Leg 76. Init. Rep. DSDP, Leg 76, Norfolk to Fort Lauderdale 367–375. https://doi.org/10.2973/dsdp.proc.76.107.1983.

Li, B.H., 2012. Kinetic energy correction coefficient αk: its theory value and experimental validation analysis of Bernoulli's equation in fluid dynamics. J. Wuhan Univ. Technol. 34 (5), 35–39. https://doi.org/10.3963/j.issn.1671-4431.2012.05.008.

Li, C., Xie, H., Gao, M., et al., 2021b. Novel designs of pressure controllers to enhance the upper pressure limit for gas-hydrate-bearing sediment sampling. Energy 227, 120405. https://doi.org/10.1016/j.energy.2021.120405.

Li, J.N., Wang, J., Hu, Y., et al., 2022. Contact performance analysis of pressure controller's sealing interface in deep in-situ pressure-preserved coring system. Pet. Sci. 19 (3), 1334–1346. https://doi.org/10.1016/j.petsci.2021.11.022.

Li, J., Xie, H., Li, J., et al., 2025. A lightweight pressure- and gas-preserved coring tool for accurate gas content measurement in deep coal seams. J. Clean. Prod. 501, 145230. https://doi.org/10.1016/j.jclepro.2025.145230.

Li, X., Gang, S., Zhao, M., et al., 2021a. Development of advancing detection tool and pressure core sampler for marine gas hydrate exploration. In: ISOPE International Ocean and Polar Engineering Conference, Rhodes, Greece.

Li, X., Zhang, X., Ma, Y., et al., 2024. Design and experimental study of an improved pressure core sampler for marine gas hydrates. ACS Omega 9 (13), 14977–14984. https://doi.org/10.1021/acsomega.3c09013.

Liu, G., Jin, Y., Peng, Y., et al., 2023a. Scheme design and pressure-retaining performance analysis of macrobiological sampler in the full-ocean-depth operating environment. J. Atmos. Ocean. Technol. 40 (1), 85–97. https://doi.org/10.1175/JTECH-D-22-0062.1.

Liu, G., Jin, Y., Peng, Y., et al., 2023b. Experimental study of self-locking seal structure based on full ocean depth sediment pressure retaining sampler. Appl. Ocean Res. 141, 103767. https://doi.org/10.1016/j.apor.2023.103767.

Liu, G., Jiang, S., Jin, Y., et al., 2025. Mechanism of low-disturbance and high-pressure-retaining sampling of seafloor sediments at 10000-meter depth and its laboratory experiment and on-site sea trials. Int. J. Min. Sci. Technol. https://doi.org/10.1016/j.ijmst.2025.06.001.

Liu, X., Wei, Z., Wang, L., et al., 2011. Particle-wall adhesion behavior in labyrinth emitter obeying energy balanced adhesion theory. J. Xi'an Jiaot. Univ. 45 (10), 120–124. https://doi.org/10.3321/j.issn:0253-987X.2009.09.026.

Luo, Y., Peng, J., Sun, M., et al., 2015. An ice-valve-based pressure-coring system for sampling natural hydrate-bearing sediments: proof-of-concept laboratory studies. J. Nat. Gas Sci. Eng. 27, 1462–1469. https://doi.org/10.1016/j.jngse.2015.10.011.

Mukherjee, P., Peres, J., Hayat, L., et al., 2019. First-ever large diameter fully captured & retained pressurized core and in-situ analysis with slow depressurization-pilot case on giant burgan reservoir. In: Abu Dhabi International Petroleum Exhibition & Conference. https://doi.org/10.2118/193021-MS.

Qin, H.W., Gu, L.Y., Li, S.L., et al., 2005. Pressure tight piston corer-A new approach on gas hydrate investigation. China Ocean Eng. 1 (19), 121–128. https://doi.org/10.3321/j.issn:0890-5487.2005.01.011.

Radich, A.S., Magalhães Filho, S.C., Borges, R.F.O., et al., 2023. Real-time control and monitoring of drilling fluids density by fuzzy-based control system. Geoenergy Sci. Eng. 222, 211421. https://doi.org/10.1016/j.geoen.2023.211421.

Schultheiss, P., Holland, M., Humphrey, G., 2009. Wireline coring and analysis under pressure: recent use and future developments of the HYACINTH system. Sci. Drill. (7), 44–50. https://doi.org/10.2204/iodp.sd.7.07.2009.

Schultheiss, P., Holland, M., Roberts, J., et al., 2017. Advances in wireline pressure coring, core handling, and core analysis related to gas hydrate drilling investigations. In: 9th International Conference on Gas Hydrates. Denver, USA.

Thomas, C., Phillips, S.C., Flemings, P.B., et al., 2020. Pressure coring operations during the University of Texas-Gulf of Mexico 2-1 (UT-GOM2-1) hydrate pressure coring expedition in green Canyon Block 955, northern Gulf of Mexico. AAPG Bull. 104 (9), 1877–1901. https://doi.org/10.1306/02262019036.

Vakkilainen, E.K., 2017. Steam-Water Circulation Design. Butterworth-Heinemann, pp. 87–114.

Wang, J., Sun, Y., Qian, D., et al., 2022a. Scheme design and performance analysis of thin-walled pressure-retaining coring tools for seafloor drills in the deep-sea operating environment. J. Pet. Sci. Eng. 208, 109790.

Wang, J., Yu, M., Qian, D., et al., 2022b. Optimisation of drainage performance of the thin-walled core barrel sealing technology for pressure preservation sampling. Ocean Eng. 250, 110996. https://doi.org/10.1016/j.oceaneng.2022.110996.

Wang, J., Yu, M., Chen, C., et al., 2023. Analysis of factors affecting the internal seawater flow performance of pressure-retaining drilling tool for seafloor drill during drilling process. Geoenergy Sci. Eng. 224, 211601. https://doi.org/10.1016/j.geoen.2023.211601.

Xie, H., Gao, M., Zhang, R., et al., 2024. Application prospects of deep in-situ condition-preserved coring and testing systems. Adv. Geo-Energy Res. 14 (1), 12–24. https://doi.org/10.46690/ager.2024.10.04.

Xie, H., Gao, X., Liu, T., et al., 2020. Electricity generation by a novel CO_2 mineralization cell based on organic proton-coupled electron transfer. Appl. Energy 261, 114414. https://doi.org/10.1016/j.apenergy.2019.114414.

Xie, H., Hu, Y., Gao, M., et al., 2023. Research progress and application of deep in-situ condition preserved coring and testing. Int. J. Min. Sci. Technol. 11 (33), 1319–1337. https://doi.org/10.1016/j.ijmst.2023.06.007.

Xie, H., Li, C., He, Z., et al., 2021a. Experimental study on rock mechanical behavior retaining the *in situ* geological conditions at different depths. Int. J. Rock Mech. Min. Sci. 138, 104548. https://doi.org/10.1016/j.ijrmms.2020.104548.
Xie, H., Liu, T., Gao, M., et al., 2021b. Research on in-situ condition preserved coring and testing systems. Pet. Sci. 18 (6), 1840–1859. https://doi.org/10.1016/j.petsci.2021.11.003.
Xu, M., Li, Y., Chen, L., et al., 2022. Structural design and dynamic simulation optimization of the triggering device in a pressure-holding controller for deep *in situ* coring. Appl. Sci. 12 (10), 4961. https://doi.org/10.3390/app12104961.
Yang, L., Sun, W., Luo, J., et al., 2014. Study and application of GWY194-70BB heat and pressure preservation coring tool. Oil Drill. Prod. Technol. 36 (5), 58–61. https://doi.org/10.13639/j.odpt.2014.05.014.
Yang, L., Su, Y., Luo, J., et al., 2020. Development and application of GW-CP194-80A pressure-maintaining coring tool. Nat. Gas. Ind. 40 (4), 91–96. https://doi.org/10.2118/36263-PA.
Yang, Y., 2008. Application of hydromechanics theory in flow measurement. Industr. Measure. 1, 16–19.
Zheng, C., Liu, Y., Wang, H., et al., 2015. Structural optimization of downhole fracturing tool using turbulent flow CFD simulation. J. Pet. Sci. Eng. 133, 218–225. https://doi.org/10.1016/j.petrol.2015.06.006.
Zhu, H.Y., Liu, Q.Y., Wong, G.R., et al., 2013. A pressure and temperature preservation system for gas-hydrate-bearing sediments sampler. Petrol. Sci. Technol. 6 (31), 652–662. https://doi.org/10.1080/10916466.2010.531352.

Glossary

Symbols

F: Force
d: Diameter
E: Elastic modulus
k: Stiffness
Δx: Spring displacement
G: Shear modulus
e: Effective number of the spring
v: Velocity
s: Sectional area
Z: Surface potential energy
P: Local pressure
h: Head loss
g: Gravitational acceleration
Q: Pump displacement
ΔH: Sum of the distances
L: Length
Re: Reynolds number
S: Annular section area
n: Safety factor

Greek symbols

μ: Friction coefficient
α: Kinetic energy correction factor
ρ: Fluid density
λ: Frictional loss factor
ξ: Local loss coefficient
η: Kinetic viscosity
χ: Wetting perimeter
τ: Shear strength

Subscripts

lif: Lifting
R: Resistance
g: Gravity
fR: Friction resistance
hR: Hydraulic resistance
sR: Spring resistance
ss: Sealed surface
io: Inside of the O-ring groove
so: Section of the O-ring
sw: Spring wire
sm: Spring middle
a, b: Cross-sections
1–5: Cross-sections in Fig. 4
f: Frictional
l: Local
flu: Fluid
ae: Annulus equivalent
she: Shear